An aromatic dyad motif in dye decolorizing peroxidases has implications for free radical formation and catalysis

Amanda K. Chaplin[#], Tadeo Moreno Chicano[†], Bethany V. Hampshire[‡], Michael T. Wilson, Michael A. Hough, Dimitri A. Svistunenko*, Jonathan A.R. Worrall*

School of Biological Sciences, University of Essex, Wivenhoe Park, Colchester, CO4 3SQ, U.K.

*To whom correspondence should be addressed: Dimitri Svistunenko (svist@essex.ac.uk)
Jonathan Worrall (jworrall@essex.ac.uk)

Present addresses:

[#]Department of Biochemistry, University of Cambridge, 80 Tennis Court Road, Cambridge, CB2 1GA, U.K.

[†]Department of Molecular Mechanisms, Max Planck Institute for Medical Research, Jahnstraße 29, 69120 Heidelberg, Germany.

[‡]Department of Physics, University of Warwick, Coventry, CV4 7AL. U.K.

ABSTRACT

Dye decolouring peroxidases (DyPs) are the most recent class of heme peroxidase to be discovered. On reacting with H_2O_2, DyPs form a high-valent iron(IV)-oxo species and a porphyrin radical (Compound I) followed by stepwise oxidation of an organic substrate. In the absence of substrate, the ferryl species decays to form transient protein-bound radicals on redox active amino acids. Identification of radical sites in DyPs has implications for their oxidative mechanism with substrate. Using a DyP from *Streptomyces lividans,* referred to as DtpA, which displays low reactivity towards synthetic dyes, activation with H_2O_2 was explored. A Compound I EPR spectrum is detected, which in the absence of substrate decays to a protein-bound radical EPR signal. Using a newly developed version of our Tyrosyl Radical Spectra Simulation Algorithm, we show that the radical EPR signal arises from a pristine tyrosyl radical and not a mixed Trp/Tyr radical that has been widely reported in DyP members exhibiting high activity with synthetic dyes. The radical site is identified as Tyr374, with kinetic studies inferring that Tyr374 is not on the electron transfer pathway from the dye RB19, but its replacement with a Phe does severely compromise activity with other organic substrates. Our findings hint at the possibility that alternative electron transfer pathways for substrate oxidation are operative within the DyP family. In this context, a role for a highly conserved aromatic dyad motif discussed.

INTRODUCTION

Activation of oxygen for the oxidative combustion of organic matter can be achieved through its reaction with transition metal complexes leading to the formation of metal-oxo compounds that are more reactive than oxygen itself.[1] In nature, the serial reductive activation of oxygen can be facilitated through copper and iron centers in metalloenzymes.[1] One such example is the iron containing heme peroxidases, which activate oxygen through the formation of two transient high-valent iron(IV)-oxo species referred to as Compound I and Compound II.[2] Understanding the chemical nature of ferryl heme intermediates has been challenging and not without controversy.[3] Recent structural studies including X-ray[4] and neutron diffraction[3, 5] along with an X-ray free-electron laser (XFEL) approach,[6] coupled with spectroscopic methods[7] have begun to provide validated insights into the nature and reactivity of compounds I and II in heme peroxidases. Such knowledge is paramount to understanding catalysis of these enzymes as the ferryl species control the reactivity of the peroxidase towards a substrate.[3]

Dye decolourising peroxidases (DyPs) are the most recent class of heme peroxidase to be discovered with their genes widespread in bacteria and fungi.[8] DyPs lack sequence and structural similarities with classical plant and animal peroxidases. As the name indicates, DyPs can utilise H_2O_2 to oxidise a wide range of azo and anthraquinone-based synthetic dyes, substrates which are less susceptible to oxidation by members of other heme peroxidase classes. In addition, certain DyPs have been reported to oxidise phenolic lignin model compounds, thus offering the enzymatic potential for this class of heme peroxidase to assist in the deconstruction of lignocellulose biomass for downstream biofuel production.[9] Based on sequence similarities, DyPs have been placed into four sub-families (types A to D) in the peroxidase data base, PeroxiBase,[10] and more recently a structure-based sequence alignment approach has led to a reclassification into three subfamilies I, P and V.[11]

Oxidation of substrate by DyPs is achieved through the formation of the two ferryl catalytic intermediates, Compound I and Compound II. The classical Compound I is a porphyrin π-cation radical [(Fe^{4+}=O)por•+] that can be reduced by a substrate to Compound II (Fe^{4+}=O or Fe^{4+}-OH if protonated) followed by subsequent reduction to the ^{fe}rric state. In all heme peroxidases, the O-O bond heterolysis to form Compound I must be accompanied by proton abstraction and transfer.[12] The mechanism of proton movement remains a matter of debate[3, 6, 12-13], but a role for a distal His residue as an acid/base catalyst is undisputed in classical peroxidases.[12] However, in DyPs the distal His is replaced by an Asp,[14] a weaker base than a His. Several mutagenesis studies have provided conflicting views as to the role of

the distal Asp in Compound I formation, stability and reactivity in DyP members with an emerging view being the existence of mechanistic variation between subfamilies.[14-15]

Binding sites for small substrates to classical heme peroxidases are found at either the δ or γ edges of the heme, with a short distance to the heme facilitating electron transfer (ET) to the ferryl species.[16] In contrast structural data for DyPs reveal that small substrates are unable to directly access the heme pocket but instead bind at the entrance to a water filled channel connecting the enzyme surface to the heme. [17] These bound substrates communicate with the heme's γ edge via a network of hydrogen bonds (H-bonds) thus ensuring rapid ET to the ferryl heme over a distance of ~5 Å.[17] An alternative mechanism of substrate oxidation by heme peroxidases was first identified in the fungal lignin (LiP) and versatile (VP) peroxidases.[18] These enzymes utilise catalytic surface sites predominantly through the oxidation of solvent exposed Trp residues to tryptophanyl radicals by long range ET (LRET) from Compounds I and II.[19]. An exception is the LiP from *Trametopsis cerviva* in which the catalytic Trp conserved in all other LiPs is replaced with a Tyr residue, which can form a catalytic protein radical.[20] A LRET mechanism to abstract an electron from a bulky substrate has been proposed in DyPs with early studies identifying a Tyr residue as a likely radical site.[21] A tyrosyl radical has also been implicated in through-protein ET of Compound II reduction in myoglobin (Mb) and haemoglobin (Hb) following activation with H_2O_2.[22] Electron Paramagnetic Resonance (EPR) spectroscopy on DyPs have identified a protein-bound radical signal with a spectral line shape that is interpreted to arise from a mixed Trp/Tyr radical species.[23]

Streptomyces lividans is a soil dwelling microbe that contains three dye decolourising-type peroxidases (Dtp), of which two belong to the A-type subfamily (DtpA and DtpAa; new subclass I) and one to the B-type subfamily (DtpB; new subclass P). The physiological substrates of these DyPs are yet to be identified. However, a functional role for DtpA in morphological development of *S. lividans* and a cooperative function with the copper radical oxidase GlxA, have been reported.[24] The catalytic cycle and ferryl intermediates of DtpA have been characterised through absorption spectroscopy and the oxidation kinetics of small and bulky substrates, including the anthraquinone dye, Reactive Blue 19 (RB19), have been determined.[25] From these studies it was notable that DtpA displayed poor reactivity with RB19 compared with another A-type DyP.[15a, 23b]

In the present study, we combine low dose X-ray crystallography, EPR spectroscopy and optical stopped-flow kinetic measurements to characterise the intermediates present in the

catalytic reaction cycle of DtpA. The validated, predominately ferric structure of DtpA reveals a short Fe(III)-OH_2 bond and an extensive H_2O network in the distal pocket. On activation by H_2O_2, an EPR spectrum assigned to a Compound I species and a protein-bound radical are detected and the kinetics of their formation and evolution are analysed. Our previously reported Tyrosyl Radical Spectra Simulation Algorithm (TRSSA)[26] (abbreviated here as TRSSA-Y, to clearly distinguish it from a similar algorithm for tryptophanyl radicals, TRSSA-W[27]) has been developed further and used to assign the protein radical species in DtpA to a sole Tyr residue with its identity (Tyr374) validated though site-directed mutagenesis. The latter approach, together with detailed kinetic studies imply an important role for Tyr374 in oxidation of 2,2-azinobis(3-ethylbenthiazoline-6-sulfonic acid) (ABTS), but not for the synthetic dye RB19. We propose that for efficient oxidation of synthetic dyes, an ET pathway is operable in A-type DyPs that involves a surface *Trp* residue that forms part of a *Trp*-Trp/Tyr dyad, a steric motif which optimises radical stability, and is conspicuous by its absence in DtpA.

RESULTS

X-ray structure of the ferric 'resting state' of DtpA

The crystal structure of DtpA has been determined previously with the heme in the oxy-ferrous state as spectroscopically validated *in situ*.[28] Here we describe the spectroscopically validated ferric structure of DtpA (Fig. 1A and Fig. S4) at a resolution of 1.41 Å (Table 1). X-ray photo-reduction of the heme was mitigated by performing a low-dose helical data collection procedure, and the redox state monitored along the exposed pathway using *in situ* UV-vis microspectrophotometry (Fig. S5). Due to the off-axis geometry of the microspectrophotometer light path relative to the X-ray beam, together with differing focal spot and X-ray beam sizes, it is inevitable that unexposed regions of the crystal will contribute to the observed absorption spectrum. However, the presence of the 630 nm band (Fig. S5B) indicative of a ferric high-spin (HS) heme and the absence of the intense α/β peaks characteristic of the photo-reduced form of DtpA [28] in any of the measured spectra following X-ray exposure in the helical data collection gave confidence that a data set representing a predominately ferric form of the enzymes was collected.

In the distal heme pocket a single, well ordered axial H_2O molecule (W1) is tightly bound (1.98 ± 0.096 Å, B-factor 11.5 $Å^2$) to the heme iron (Fig. 1B). W1 forms the starting point for a chain of well ordered, full occupancy H_2O molecules, interacting through strong H-bonds (2.5 to 2.8 Å) (Fig. 1B), which lead away from distal site towards a surface exposed

channel entrance (*vide infra*). W1 H-bonds to the Nη1 atom of Arg369 and to W2 (B-factor 12.8 Å^2), which in turn H-bonds to W3 (B-factor 11.7 Å^2) and the Oδ2 atom of Asp251 (Fig. 1B). W4 (B-factor 16.3 Å^2) H-bonds with W3 and the Oδ1 atom of Asp251 and W5 (B-factor 16.0 Å^2), which is positioned at the solvent exposed entrance (Fig. 1B). The network of H_2O molecules connecting the distal heme site to bulk solvent may therefore provide a conduit for proton transfer and access for facile diffusion of H_2O_2. Notably, the DyP-conserved residues, Asp251 and Arg369, form a salt bridge between the Oδ1 atom of the Asp and the Nη1 atom of the Arg (3.1 Å) (Fig. 1B red dashed line). Arg369 is also involved in two further polar interactions with the O2A atom of the inwardly pointing heme-7 propionate substituent via H-bonds from the Nη1 and Nη2 atoms (see Fig. 1 caption for full details). A superposition of the heme environment in the ferric structure with that of the oxy-ferrous structure[28] is given in Fig. 1C. Additional verification for the ferric redox state is provided by the well-ordered active site pocket. Partially photo-reduced mixed-state structures (e.g. 5MJH)[28] typically display multiple partially-occupied H_2O networks corresponding to the mixed redox/ligand states and consequently disordered or 'streaky' electron density features in the channel. Arg369 adopts a similar position in both the oxy-ferrous and ferric structures, while Asp251 shows a small movement to accommodate the oxygen ligand (Fig. 1C). Small differences in the conformations of Phe390 and Pro304 are also evident (Fig. 1C).

Electrostatic surface potentials calculated at pH 7 for DtpA are shown in Fig. 1D, with two surface access points forming tunnels to the heme pocket (*a* and *b*) indicated. The entrance to tunnel *a* is located side-on to the heme propionate-6 substituent and has a highly electropositive surface entrance formed by the side chains of two Arg residues. Two H-bonded H_2O molecules connect the O2A atom of the heme propionate-6 substituent with bulk solvent, with a heme to surface distance of 5.4 Å. A similar surface site with an ET route to the heme propionate-6 substituent has been identified in other DyPs[29]. The second tunnel entrance, *b*, is less charged and leads directly to the distal side of the heme and houses the H-bonded H_2O chain consisting of W1-W5, discussed above. This tunnel may therefore be more favoured for H_2O_2 access. The direct distance from W1 (bound to the ferric heme) to W5 at the surface entrance is 6.7 Å. Tunnel entrances have maximum diameters of ~ 9 and 7 Å for *a* and *b*, respectively, and thus, whilst both tunnels would be viable to enable access of H_2O_2, bulky substrates such as synthetic dyes or lignin polymers would not be accommodated.

Compound I and a protein-bound radical are detected in DtpA following H_2O_2 activation

The low temperature EPR spectrum of ferric DtpA is shown in Fig. 2A and reveals a typical HS ferric heme with two components at the g=6 region (perpendicular) and one component at g=2. In addition to an almost axial form with two perpendicular components having very close g-factors around g=5.84, the 'wings' of the EPR signal reveal two HS ferric heme forms with distinct rhombicities, *i.e.* different distances between the two perpendicular g-factor components, which are more pronounced at pH 7 (Fig. S6) where the axial form dominating at pH 5 is now absent.

Addition of H_2O_2 to ferric DtpA results in a fast and transient decrease of the ferric heme form (Fig. 2B) and a simultaneous appearance of a free radical EPR signal at g=2 (Fig. 2C and S7). An unusual feature is a small narrow peak to the right of the free radical signal, that exists transiently over the initial 0.5 min of the reaction (Fig. 2C). The line shapes of protein-bound radical EPR spectra are usually resolved to a greater degree at a lower microwave power and this is the case here with DtpA (Fig. 2D). The specific line shape of the radical signals in the reaction time interval of 1 to 6 min strongly suggests that the highest contribution to these signals arises from a tyrosyl radical (*vide infra*). Interestingly, the narrow peak to the right of the free radical signal is not seen at a lower microwave power of 0.05 mW (Fig. 2D), indicating that this feature and the free radical EPR signal have very different microwave power saturation behavior. Indeed, the free radical region of the EPR spectrum studied at a range of microwave power values (Fig. 3A) shows a dramatic change in relative contributions of the free radical and the species with narrow peak, the latter showing no saturation whatsoever (linear on square root of power) with microwave power (Fig. 3A). This failure to saturate up to 200 μW is uncharacteristic of protein-bound radicals and thus indicates the presence of a factor that significantly speeds up the paramagnetic centre relaxation – e.g. a metal ion. The EPR signal (Fig. 3A, *inset* left) exhibits a very strong asymmetry of the line shape (strong g-factor and line width anisotropies), which is also not typical of protein-bound radicals. Instead these features are typical of a classical Compound I [$(Fe^{4+}=O)por^{\bullet+}$] and are a consequence of the exchange interaction part in the Hamiltonian $\overrightarrow{S} \cdot \overleftrightarrow{\boldsymbol{J}} \cdot \overrightarrow{S'}$ between spin S = 1 of the ferryl iron and spin S'=1/2 of the π-cation radical of the porphyrin.[30] Also, the microwave power dependence of this signal shows no saturation up to the highest power (Fig. 3A, *inset* right), which is also typical of Compound I. Therefore, we propose that the EPR signal with the sharp maximum at g=1.9996 present between 0.07 to 0.5 min following H_2O_2 activation arises from a classical Compound I species [$(Fe^{4+}=O)por^{\bullet+}$]. Thus, at the earliest

time points two species are observed in the free radical region of the EPR spectrum assigned to a classical Compound I and its decay product, a protein-bound radical.

Time dependence of the reaction intermediates monitored by EPR spectroscopy

Optical spectroscopy has revealed that on mixing H_2O_2 with DtpA the HS ferric species decays and a classical Compound I [$(Fe^{4+}=O)por^{\bullet+}$] species reaches full occupancy in milliseconds.[25] The kinetics of the 3 paramagnetic centres assigned in DtpA by EPR spectroscopy following activation by H_2O_2 thus miss the kinetics of Compound I formation but reveal, as expected, that i) Compound I is at a maximal concentration when the HS ferric heme form is at its minimum and ii) the increase of the free radical concentration and the decrease of Compound I concentration are contemporaneous (Fig. 3B, C & D). The maximum observed concentration of Compound I has been estimated to be 0.44 μM at 30 s before it decays (Fig. 3C). An estimate that amounts to only 10-15% of the total HS ferric form (40 μM) present before H_2O_2 addition. Reasons for this concentration discrepancy are addressed in the Discussion. However, the decay of Compound I (0.44 μM) yields 0.5 μM of protein-bound free radical indicating a strict stoichiometric relationship between these two species.

Simulation of the protein-bound radical signal reveals a tyrosyl radical

The line shape of the free radical EPR signal evolves over the reaction time from a partly resolved signal, best seen at low microwave power at 1-3 min (Fig. 2D), to a featureless singlet (9 min). Such a change in the EPR line shape with time has been noted before for protein-bound radicals and results from the migration of a free radical character from a specific site on a protein to several different sites facilitated by intermolecular protein-protein reactions.[31] The 'featureless' EPR singlet is therefore assigned to a superposition of different EPR line shapes from multiple amino acid radicals (the multiple protein-bound radical hypothesis [31]). Therefore, the EPR signal line shape detected over the reaction time 1-3 min, before it evolves into a featureless singlet (Fig. 2D), is caused by a distinct free radical species, and a simulation of its EPR signal can inform on the amino acid residue that hosts the radical character. With the hypothesis that the radical is on a Tyr, TRSSA-Y.v2 was used to simulate the EPR radical signal present at 3 min following H_2O_2 activation. For the values of the TRSSA-Y.v2 input of the spin density on the Tyr C1 atom $\rho_{C1} = 0.38$ and the ring rotation angle $\theta = 56^{o}$ (Fig. 4A), the algorithm generated the parameters reported in Table S1, which were used to simulate the spectrum shown in Fig. 4B. The good fit to the experimental spectrum strongly supports the

hypothesis that the protein-bound radical is on a Tyr residue. It should be noted that from the symmetry consideration,[32] the EPR simulation will be identical for the complemented angle θ = 62° (Fig. 4B).

Tyr288 and Tyr374 are radical site contenders

DtpA possesses three Tyr residues, Tyr288, Tyr374 and Tyr437 (Fig. 4C) which have solvent accessible surface areas calculated in PyMOL of 5.6, 0.0 and 21.1 Å^2, respectively. Using the phenol ring rotation angle database,[33] θ for the Tyr residues in chains A and B of the asymmetric crystallographic unit of the ferric DtpA structure have been determined. Table 2 reports the average θ value over chains A and B for each Tyr along with their *difference* from the angle obtained from the simulation. The results in Table 2 suggest that each of the 3 Tyr residues has a possibility of being the radical site, which based on increasing *difference*, results in a hierarchy of high-to-low as follows: Tyr288 (1° difference with the 56° simulation) >Tyr374 (2.4° difference with the 62° simulation) >Tyr437 (2.7° difference with the 62° simulation) > Tyr437 (3.3° difference with the 56° simulation) >Tyr374 (3.6° difference with the 56° simulation). The possibility of the radical being on Tyr288 with a spectrum that can be simulated for the 62° rotational conformation can be disregarded as the difference of 7° between the simulation and structure derived angles is too large. All three Tyr residues are located on the distal side of the heme (Fig. 4C) and their positions relative to surface electrostatic potential are indicated in Figure 1D. Distances to the heme iron vary in the order Tyr437 (35 Å) > Tyr288 (20 Å) > Tyr374 (15 Å) and it is noted that the value of θ for Tyr437 is found with the least accuracy as the values in the two chains in the crystallographic asymmetric unit differ by 3.9°. Therefore, based on distance and the increasing *difference* outlined in the above hierarchy, Tyr437 is the least favoured radical site. On the contrary, Tyr288 and Tyr374 are closer to the heme and have significantly smaller uncertainty in θ as derived from the two chains. Tyr288 has a closer θ angle to one of the two found from the simulation (only 1° away from 56°) but Tyr374 (2.4° away from 62°) is closer to the heme and has a smaller uncertainty in θ.

Site-directed variants identify Tyr374 as the radical site

To verify the location of the tyrosyl radical observed by EPR spectroscopy, the Y288F, Y374F and Y437F variants of DtpA were constructed. UV-vis absorbance spectra of the purified variants showed no wavelength differences for assigned peak maxima in the ferric resting state

or on generating Compound I by activation with H_2O_2 at pH 5.0 compared to the WT DtpA.[25] Following addition of 1 equivalent of H_2O_2 to the Tyr variants, the spectral decay of Compound I was monitored by absorption spectroscopy. For the Y288F and Y437F variants the decay of Compound I to the ferric resting state spectra in the absence of a substrate was observed on a similar time scale ($t_{1/2}$ ~ 2.5 min) as for the WT DtpA.[25] In contrast the Y374F variant displayed a longer-lived Compound I species with a significantly slower decay to the ferric resting state ($t_{1/2}$ > 10 mins).

Time series samples of the Tyr variants following activation with H_2O_2 for EPR analysis were prepared and studied in an identical manner to WT DtpA (Fig. S8). For all Tyr variants, a rapid initial decrease of the ferric heme concentration (quantified and displayed in Fig. S9) was observed. However, for the Y374F variant the EPR spectrum in the free radical region is essentially absent (Fig. 5A) and replaced by an additional line consistent with Compound I (Fig. 5B). Using a lower microwave power clearly demonstrates that the WT, Y288F and Y437F proteins, following activation with H_2O_2 and frozen at the time point of maximal concentration of free radicals (90 s, see Fig. S9), exhibit a free radical with persistently the same EPR line shape, thus strongly suggesting the same species. In contrast, the Y374F spectrum is lacking a free radical signal, with a Compound I species persisting, which is consistent with the observations by absorbance spectroscopy of a 'longer-lived' Compound I species for this Tyr variant. Thus, while the free radical EPR spectrum simulation ambiguously indicates that all three Tyr residues might be the host of the radical, with the likeliness being Tyr288 > Tyr374 >> Tyr437, site-directed mutagenesis strongly points to Tyr374, as its replacement by a Phe eliminates the free radical EPR spectrum, while replacement of either Tyr288 or Tyr437 affects the radical yield but not the radical species observed in the WT DtpA.

Steady-state and transient kinetic studies of the DtpA Tyr variants reveal Tyr374 to be important for ABTS oxidation

The rate of Compound I formation in the Tyr variants was monitored by stopped-flow absorbance spectroscopy. A linear increase in k_{obs} with increasing H_2O_2 concentrations was observed for each variant enabling second-order rate constants (k_1) to be determined (Table 3), with values essentially identical to WT DtpA (Table 3). Using ABTS as substrate, steady-state kinetics of the Tyr variants were assessed. In all cases Michaelis-Menten behaviour was observed and the determined k_{cat} and K_m values are reported in Table 3. For all variants, k_{cat} is least affected whereas K_m shows significant increase, with the largest difference being observed

for the Y374F variant with respect to WT DtpA (Table 3). This results in an overall 5.5-fold decrease in catalytic efficiency (k_{cat}/K_m) (Fig. 6A). Transient stopped-flow kinetics using ABTS as substrate were also carried out. On mixing pre-formed Compound I with ABTS, two distinct kinetic phases were observed at 420 nm for all Tyr variants, with a fast phase coinciding with an increase in absorbance followed by a slow bleaching. Identical behavior has previously been reported for WT DtpA and has been assigned as the fast reduction of Compound I to Compound II and the slower reduction of Compound II to the ferric resting state.[25] Pseudo-first order rate constants (k_{obs}) for each phase were found to be ABTS concentration dependent enabling second order rates constants (k_2 and k_3) to be determined (Table 3). It is apparent from Table 3 that each Tyr variant has a small but significant effect on the k_2 rate constant (Compound I to II). Notably, the k_3 values observed are comparable under the same conditions to the k_{cat}/K_m values determined under steady-state conditions (Fig. 6A). Together, the steady-state and transient kinetics corroborates the proposition that reduction of Compound II to the ferric form is the rate-limiting step and shows that with ABTS as substrate, Tyr374 plays a significant role.

Further kinetic investigations with WT DtpA and the Tyr variants were carried out with the anthraquinone-based dye, RB19. As with ABTS, two phases, a fast and a slow, were observed and assigned to reduction of Compound I to II and Compound II to ferric, respectively. In contrast to ABTS, however, a non-linear dependence on k_{obs} values for both kinetic phases were observed (Fig. 6B), k_2 approaching a value of ~30 s^{-1} and k_3 ~ 0.09 s^{-1} for the WT. This approach to limiting rates was not discerned from an earlier study,[25] presumably because the rates measured on that DtpA preparation did not approach these limiting values. As opposed to the results with ABTS, the removal of Tyr374 has a relatively small effect on kinetics of the transitions from Compound I to II and Compound II to ferric resting state (Fig. 6B).

DISCUSSION

Deciphering the electronic properties of the resting state HS ferric, the transient high-valent iron(IV)-oxo species and the protein-bound free radical in the DyP family is important for understanding these species reactivity for the overall biocatalysis of these heme enzymes. X-ray crystal structures of several A-type DyPs have been reported. With the exception of the oxy-ferrous structure of DtpA,[28] none of the deposited DyP structures report validation of the heme iron redox state. Our validated high-resolution predominately ferric structure of DtpA has a well-defined density feature axial to the heme iron (Fig. 1B), which we have modelled as

a H_2O molecule with a bond distance to the iron of 1.98 ± 0.096 Å. A H_2O bound HS ferric heme is consistent with the 630 nm band observed in the absorbance spectrum of the crystal (Fig. S5B), a band also present at room temperature in solution.[25] In other peroxidases, where the redox state of the heme iron has been validated by single crystal spectroscopy, Fe(III)-OH_2 interactions under cryo-conditions (100 K) of 2.33 Å for cytochrome c peroxidase (CcP) and 2.08 Å for ascorbate peroxidase (APX), have been reported [16b, 34]. Thus, in DtpA a relatively short Fe(III)-OH_2 interaction is found. Estimation of bond length error is critical for comparison of structures where radiation damage is likely to affect the structure and when comparing structures of differing resolution. A further consideration is the relationship between structural and spectroscopic data measured at different temperatures (e.g. 100 K and room temperature). In this study, the similarity between single crystal spectra at 100 K and room temperature solution spectra are reassuring that the electronic structure is not unduly affected by sample temperature. Further studies to elucidate the structural nature of Compound I and/or Compound II of DtpA, to complement the EPR spectroscopy data are now required and it will be of interest to compare these with studies on the ferryl heme structure of class I peroxidases, such as CcP and APX.[4-6, 13] In relation to this, the solvent structure in the distal pocket of peroxidases is considered important for movement of protons to generate the ferryl states.[12] It is noted that in the ferric DtpA structure, an intricate and extensive well-ordered H_2O network in the distal pocket exists, enabling the iron to communicate with bulk solvent and both the Asp and Arg residues (Fig. 1B and C), both of which are implicated in being important for the generation and stability of catalytic ferryl species.

Absorbance spectroscopy reveals a 'classical' Compound I [(Fe^{4+}=O)por•+] spectrum for DtpA following addition of one equivalent of H_2O_2,[25] in keeping with all other peroxidase classes. In contrast, the EPR spectrum of Compound I is found to vary significantly among numerous peroxidases and globins for which it has been reported.[30, 35] The variation is attributed to the changeable contribution of the exchange parameter **J** to the spin Hamiltonian that describes the interaction between the ferryl iron electron spin S=1 and porphyrin cation radical spin S'=1/2. The line shape of the DtpA EPR signal assigned as Compound I is similar to that of the Compound I spectrum in HRP, the latter being interpreted as exhibiting an extremely weak exchange parameter, with the simulation requiring that the zero-field splitting (J/D) be assigned both ferromagnetic and antiferromagnetic values.[30a] We note that the type of asymmetry of the EPR lines of Compound I in both HRP and DtpA spectra implies that the antiferromagnetic exchange has a greater contribution than that of the ferromagnetic one, since

the two effective perpendicular *g*-values should be somewhere to the right of g=2. Indeed, those g-values, in the antiferromagnetically exchanged Compound I of chloroperoxidase were identified as 1.73 and 1.64.[30b]

The concentration of Compound I in the frozen DtpA samples as detected by low-temperature EPR spectroscopy, constitutes a small part (10-15%) of the total peroxidase concentration (Fig. 3C). This is in contradiction with the room temperature optical absorbance spectroscopy, when the conversion of ferric DtpA to Compound I is rapid ($k = 9\times10^6\ M^{-1}\ s^{-1}$) and Compound I is relatively stable ($t_{1/2}$ = 2.5 min, in absence of substrate).[25] Quantitative measurements by low temperature EPR spectroscopy are affected by solution freezing,[36] with the local reactant concentrations changing dramatically with the movement of the liquid to solid phase separation.[37] As a result, Compound I may be rapidly reduced gaining electrons from intermolecular interactions, in essence an enhanced auto-reduction process that is promoted during freezing. Under the conditions employed here, with excess H_2O_2, Compound I would enter a steady-state (auto-reduction quenching Compound I and H_2O_2 regenerating it). As DtpA turns over, the availability of electrons decreases and hence the steady-state would move towards an increased population of Compound I. Indeed, in line with this expectation, we observe a statistically significant gradual increase in the concentration of Compound I between 4 and 30 s (see inset Fig. 3C). Once H_2O_2 is exhausted, Compound I decays leading to the protein-bound radical formation and does so over 2-3 mins, a time period already identified by optical spectroscopy as the time course of the decay of Compound I.[25] Similar kinetic profiles to those shown in Fig. 3C and D have been reported for protein-bound radicals.[37-38] The pioneering work of Winfield and colleagues, who have investigated the kinetics of the protein-bound radical formed through the reaction of H_2O_2 with Mb is the most notable example.[39] In their study, the concentration of the radical in Mb executes a trajectory analogous to that observed here for Compound I (see inset Fig. 3C), *i.e.* a rapid increase in concentration before the first time point, followed by a local min/max in the overall decrease.

DtpA has 3 Tyr and 6 Trp residues. The simulation of the EPR spectrum of the primary free radical in DtpA, assisted by the new version of TRSSA-Y. v2, proves it can be accurately represented by a sole Tyr radical species with no evidence to suggest the presence of a Trp radical. This is in contrast to previous reports for the A-type *Thermomonospora curvata* DyP (*Tc*DyP) (3 Tyr and 7 Trp)[23b] and the fungal D-type DyP from *Auricularia auriculajudae* (*Aau*DyP) (7 Tyr and 4 Trp),[23a] where the protein-bound radical signal formed after activation with H_2O_2 has been attributed to arise from Trp and Tyr residues. A combination of TRSSA-Y. v2 and site-directed mutagenesis identified Tyr374 as the radical site in DtpA, with removal

leading to a longer-lived Compound I EPR signal. Interestingly, Tyr374 is located at the same side of the heme, opposite to the propionates, and at a similar distance to the iron, as a Tyr residue conserved in several globins shown to host a protein-bound radical.[26, 40] [41] [42] [43] [44]

Tyr374 is relatively well conserved across the DyP sub-families and it is structurally homologous to Tyr332 and Tyr337 in *Tc*DyP and *Aau*DyP, respectively, which are the Tyr residues implicated in the mixed Trp/Tyr radical EPR signal observed in these two DyPs.[23] In *Tc*DyP, Trp263 and Trp376 in addition to Tyr332 are proposed as radical sites, with Trp263 conserved in all A-type sequences, including DtpA (Trp301). For *Aau*DyP, Trp377 has been assigned as the radical site and is not conserved in A-type DyPs. Therefore, DtpA stands out in that the protein radical that evolves from decay of Compound I in the absence of substrate is a pristine tyrosyl radical, despite the presence of the homologous Trp residue (Trp263) identified as a radical site in *Tc*DyP.[23b] A reason for this may stem from the absence in DtpA of the second Trp site, Trp376 that is present in *Tc*DyP.[23b] From a structural perspective, the Trp263 and Trp376 dyad in *Tc*DyP adopts a conformation in which the indole side chains are perpendicular to one another, with a closest distance of 3.6 Å (Fig. 7). Recent work on the radical copper oxidase, GlxA, has led to the idea that a transfer of free radical character between two aromatic residues is facilitated by a steric arrangement whereby the atoms with high spin density in a free radical state are in closest proximity.[27] In free radicals of aromatic residues, high and low spin densities alternate around the ring: high spin densities are found on C1, C3 and C5 and low spin densities – on C2, C4 and C6 on the phenoxyl ring of a Tyr radical. Similarly, in Trp radicals, high spin densities are on N1, C3, C5 and C7 atoms on the indole ring.[45] We note that the closest distance of 3.6 Å between Trp263 and Trp376 in *Tc*DyP is between the atoms of high spin densities, if these residues were in a free radical state; C5 of Trp263 and C3 of Trp376 (Fig. 7). Therefore, this perpendicular steric arrangement of the two Trp residues could provide a type of coupling that allows free radical transfer/stabilisation and its detection by EPR spectroscopy. In DtpA, however, Trp376 is replaced with a non-redox active phenylalanine (Phe417) and this disrupts the redox coupling or capacity to stabilise a radical (Fig. 7). Furthermore, in other A-type DyP sequences a Tyr residue is often found to substitute for Trp376 and thus a redox dyad motif is maintained. Therefore, although it is conceivable that a radical could form on the conserved Trp301 in DtpA (equivalent to Trp263 in *Tc*DyP) the absence of the stabilising second Trp (or Tyr) diminishes its lifetime and thus detection and ultimately reactivity towards substrates.

With ABTS as substrate, Tyr374 affects the rate of the second ET step, namely Compound II to the ferric resting state as implied from both the steady-state and transient

kinetic studies (Fig. 6A). Whilst Tyr374 is not surface exposed it would seem feasible that it participates in the ET from the ABTS binding site to the heme and thus a case can be made for Tyr374 being one of the residues that form a through protein ET pathway – the one employed in ABTS oxidation (Fig. 7). On the other hand, the radical Trp residues identified in *Tc*DyP and *Aau*DyP are highly solvent accessible and their removal causes a decrease in catalytic efficiency by > 50 % relative to the respective WT proteins with RB19 (Fig. 7).[23] Interestingly, replacement of Tyr377 in *Aau*DyP, which is structurally homologous to Tyr374 in DtpA, with a Ser, results in a 2-fold decrease in catalytic efficiency with ABTS compared with the WT protein but no difference in catalytic efficiency with RB19 is observed.[23a] Such behavior mirrors that of the Y374F variant of DtpA, where a more pronounced 5.5-fold decrease in catalytic efficiency is observed (Fig. 6A). Furthermore, we note that DtpA has a ~ 10,000-fold lower catalytic efficiency with RB19 compared to *Tc*DyP.[23b] Therefore, we propose that radical sites on DyPs and the intermolecular ET pathways they serve to represent can be utilized by different substrates with Trp residues seemingly favored by RB19. Moreover, the absence of a Trp dyad in DtpA leads to an undetectable level of radical population of Trp301, which correlates with the poor catalytic activity observed for this A-type DyP with RB19.

EXPERIMENTAL SECTION

Site-directed mutagenesis, over-expression, purification and sample preparation of DtpA

The Y288F, Y374F and Y437F variants of DtpA were constructed as described in Supplementary Information. Wild type (WT) and DtpA variants were over-expressed in *Escherichia coli* and purified as previously reported.[24] Concentrations of purified DtpA samples were determined spectrophotometrically using a Cary 60 UV-visible spectrophotometer and an extinction coefficient (ε) at 280 nm of 37,470 M^{-1} cm^{-1} for WT protein and 35,980 M^{-1} cm^{-1} for the Tyr variants.[25] Stock DtpA samples were prepared and stored in 10 mM sodium acetate pH 5.0, 150 mM NaCl.

Crystallisation and structure determination

Crystals of ferric DtpA were grown at pH 5.5 and cryo-protected as described previously.[28] Low dose X-ray diffraction data for the ferric species were measured to 1.41 Å resolution at 100 K using a helical data collection procedure at the ID30A-3 (MASSIF-3) beamline, European Synchrotron Radiation Facility (ESRF, Grenoble), with an X-ray wavelength of 0.9677 Å, a beam size of 15.0 x 15.0 μm^2, a flux of $7.1x10^{10}$ photons s^{-1}) and an Eiger-4M

detector (Dectris) operating at 100 Hz. The ESRF on-line micro-spectrophotometer[46] was used to record the optical absorbance spectrum of the DtpA crystal (350 x 200 x 50 μm), in-situ at the beamline, before any X-ray exposure at pre-defined points along the helical trajectory of 300 μm, and confirmed to be in the ferric state. A combined halogen-deuterium lamp (DH2000-BAL, Ocean Optics) was used as the light source and this was focused into an optical spot size of 25 μm in diameter at the crystal. Spectra were measured over the range 350 to 800 nm using a HR2000 spectrograph with CCD detector (Ocean Optics) controlled using the *SpeCuBE* software package[46]. Data were processed in *SpectraSuite* (Ocean Optics). Each spectrum was the result of 10 accumulations of 200 ms exposures. Following acquisition of the diffraction data (total experimental time 14 s), absorbance spectra at these positions were re-collected to assess the extent of heme reduction induced by the X-ray beam. Diffraction data were automatically processed by EDNA[47] and scaled and merged using Aimless[48] in the CCP4i2 suite. The ferric structure was refined from a starting model of the oxy-ferrous DtpA structure[28] (PDB entry 5map). Refinement of the structure was carried out using Refmac5,[49] with model building between refinement cycles in Coot.[50] Riding hydrogen atoms were added when refinement of the protein atoms had converged. The structure was validated using the Molprobity server,[51] the JCSG Quality Control Server and tools within Coot.[50] A summary of data collection and refinement statistics are given in Table 1. X-ray absorbed dose was estimated using Raddose-3D,[52] using the translation option for helical collections. An estimate of bond length error for the iron-water bond was derived using the Online_DPI server[53] based on the estimated coordinate error for the two coordinated atoms.

H_2O_2 activation of DtpA samples for EPR measurements

H_2O_2 (Sigma-Aldrich) solutions were prepared from a stock with the final concentration determined spectrophotometrically at 240 nm using an ε of 43.6 M^{-1} cm^{-1}. Two procedures were used to create a time series of DtpA samples following activation by H_2O_2. All time series were prepared with WT DtpA and variants in 10 mM sodium acetate pH 5.0, 100 mM NaCl. The first procedure required the addition of a stock solution of H_2O_2 (~ 10 mM) to a DtpA sample to give a 1:10 ratio (DtpA:H_2O_2), from which an aliquot was drawn and frozen in methanol kept on dry ice (~195 K). This method provided the freezing time (*i.e.* the reaction time) from 11 s and upwards. The second procedure to enable sub 10 s sample preparation required the stock H_2O_2 solution to be inserted into the tip of a needle used to draw the DtpA

sample from the EPR tube into a syringe which was subsequently loaded back to the EPR tube and frozen, providing freezing times from 4 s.

EPR spectroscopy

Wilmad SQ EPR tubes (Wilmad Glass, Buena, NJ) with OD = 4.05±0.07 mm and ID = 3.12±0.04 mm (mean±range) were used. Samples frozen in a set of these tubes yielded very similar intensities of EPR signals - with only ~1-3% random error. All EPR spectra were measured on a Bruker EMX EPR spectrometer (X-band) at a modulation frequency of 100 kHz. A Bruker resonator ER 4122 (SP9703) and an Oxford Instruments liquid helium system were used to measure the low-temperature (10 K) EPR spectra. In the microwave power saturation experiment, the EPR spectra of a blank sample (frozen water) was prepared and measured at the same set of microwave power values as the DtpA sample. The blank spectra were then subtracted from the DtpA spectra to eliminate the baseline caused by the resonator's walls, quartz insert or quartz EPR tube. Similar correction of the baseline was applied in several other EPR measurements whenever the EPR signal was weak and comparable by intensity with the background signals. To measure intensities of individual EPR signals overlaid in complex EPR spectra caused by different paramagnetic species, the procedure of spectra subtraction with variable coefficient[54] was used. Quantitative estimates of the concentrations of the paramagnetic centres were performed by comparison of the second integrals of their EPR signals with those of a 1 mM Cu^{2+} solution sample (at pH 7.0, with 10-fold excess of EDTA).

Free radical EPR spectra simulation

The EPR spectrum of the free radical formed in DtpA samples following H_2O_2 induced activation was simulated using a new version of our previously published algorithm for finding simulation parameters for tyrosyl radical EPR spectra,[26] now referred to as TRSSA-Y.v2. Both versions of TRSSA use two inputs, the tyrosyl radical phenoxyl ring rotation angle (θ) and the spin density on the Tyr C1 atom (ρ_{C1}), to generate the parameters needed to simulate a Tyr radical EPR line shape. EPR spectra simulation was performed by SimPow6[55] which uses Euler angles as means of defining orientation of the hyperfine interaction tensors (*A*) with respect to the g-tensor: for each *A*-tensor, three rotation angles are specified in a SimPow6 input, which having performed consecutively, would bring the three principal *A*-values aligned with the three principal g-values. The original TRSSA did not define these angles for the radical's methylene protons. In TRSSA-Y. v2., the Euler angles for the A-tensors of the

methylene protons are explicitly defined as functions of θ, one of the two TRSSA-Y.v2 inputs. Continuous dependences of the three Euler angles on θ have been determined from the Density Function Theory (DFT) calculations of a set of Tyr radical models (see Supplementary Information) and have been incorporated into the algorithm.

Steady-state kinetics

Steady-state assays were set-up in 1 ml cuvettes and monitored using a Hewlett-Packard 8453 diode-array spectrophotometer scanning between 190 and 1100 nm and thermostatted at 25 ºC. Each cuvette was baselined against DtpA (concentration in assay ranging between 40-300 nM) and a set concentration of ABTS (0.1-25 mM). The reaction was started by the addition of H_2O_2 to give a final concentration of 0.2 mM. A turnover rate (v, s^{-1}) defined as the initial rate normalized to the DtpA concentration was calculated from $((\Delta A/\varepsilon/t)/[DtpA])$, where ΔA is the absorbance change at the specific ABTS oxidation wavelength (436 nm), ε is the extinction coefficient of the ABTS oxidation product (29.3 mM^{-1} cm^{-1}), t is the time in seconds and [DtpA] is the total concentration of DtpA (nM) in the assay. A non-linear least square fit of the data using a Michaelis-Menten model enabled the parameters K_m and k_{cat} to be determined. Experiments were carried out in triplicate and with different batches of DtpA variant preparations.

Stopped-flow kinetics

Kinetics of the catalytic cycle of the DtpA Tyr variants at pH 5.0 were performed using a SX20 stopped-flow spectrophotometer (Applied Photophysics) equipped with a diode-array multi-wavelength unit or a single wavelength photomultiplier and thermostatted at 25 °C. Compound I formation was monitored at pH 5.0 using a solution of DtpA (5 μM after mixing), which was rapidly mixed with a series of H_2O_2 concentrations (12.5-75 μM after mixing). Reaction progress curves were taken at 406 nm and fitted to a single exponential function. The ProKinetist (Applied Photophysics) software was used to obtain pseudo-first order rate constants (k_{obs}). The reduction of Compound I was monitored for each Tyr variant by pre-loading each variant with one equivalent of H_2O_2 and rapidly transferring to the stopped-flow working syringe, before rapidly mixing with an excess of ABTS (0.125-1 mM after mixing), or Reactive Blue 19 (25-150 μM after mixing) (RB19; Sigma-Aldrich). The overall spectral transitions were first monitored using the diode array unit, followed by monitoring at a single wavelength (420 nm) to observe the formation and subsequent decay of Compound II. A

double exponential function was required to fit the data. All k_{obs} values obtained are an average of three replicates.

ACKNOWLEDGEMENTS

The award of a Silberrad Scholarship from the University of Essex to AKC is gratefully acknowledged. TMC was supported by The Leverhulme Trust award RPG-2014-355 to MAH. We acknowledge the European Synchrotron Radiation Facility (ESRF) for provision of synchrotron radiation facilities and we would like to thank David von Stetten for assistance in using beamline ID30-A3 (MASSIF-3). We also appreciate computational time granted by the EPSRC funded UK National Service for Computational Chemistry Software (NSCCS, 1996-2017), Imperial College London.

REFERENCES

[1] X. Huang, J. T. Groves, *Chem Rev* **2018**, *118*, 2491-2553.

[2] H. B. Dunford, *Peroxidases and Catalases: Biochemistry, Biophysics, Biotechnology, and Physiology*, 2nd ed., Wiley, **2010**.

[3] P. C. E. Moody, E. L. Raven, *Acc Chem Res* **2018**, *51*, 427-435.

[4] A. Gumiero, C. L. Metcalfe, A. R. Pearson, E. L. Raven, P. C. Moody, *J Biol Chem* **2011**, *286*, 1260-1268.

[5] H. Kwon, J. Basran, C. M. Casadei, A. J. Fielding, T. E. Schrader, A. Ostermann, J. M. Devos, P. Aller, M. P. Blakeley, P. C. Moody, E. L. Raven, *Nat Commun* **2016**, *7*, 13445.

[6] G. Chreifi, E. L. Baxter, T. Doukov, A. E. Cohen, S. E. McPhillips, J. Song, Y. T. Meharenna, S. M. Soltis, T. L. Poulos, *Proc Nat Acad Sci USA* **2016**, *113*, 1226-1231.

[7] H. Kwon, O. Smith, E. L. Raven, P. C. Moody, *Acta Crystallogr D* **2017**, *73*, 141-147.

[8] [a]S. J. Kim, M. Shoda, *Appl Environ Microbiol* **1999**, *65*, 1029-1035; [b]R. Singh, L. D. Eltis, *Arch Biochem Biophys* **2015**, *574*, 56-65.

[9] G. de Gonzalo, D. I. Colpa, M. H. Habib, M. W. Fraaije, *J Biotechnol* **2016**, *236*, 110-119.

[10] N. Fawal, Q. Li, B. Savelli, M. Brette, G. Passaia, M. Fabre, C. Mathe, C. Dunand, *Nucleic Acids Res* **2013**, *41*, D441-444.

[11] T. Yoshida, Y. Sugano, *Arch Biochem Biophys* **2015**, *574*, 49-55.

[12] T. L. Poulos, J. Kraut, *J Biol Chem* **1980**, *255*, 8199-8205.

[13] C. M. Casadei, A. Gumiero, C. L. Metcalfe, E. J. Murphy, J. Basran, M. G. Concilio, S. C. Teixeira, T. E. Schrader, A. J. Fielding, A. Ostermann, M. P. Blakeley, E. L. Raven, P. C. Moody, *Science* **2014**, *345*, 193-197.

[14] Y. Sugano, R. Muramatsu, A. Ichiyanagi, T. Sato, M. Shoda, *J Biol Chem* **2007**, *282*, 36652-36658.

[15] [a]C. Chen, R. Shrestha, K. Jia, P. F. Gao, B. V. Geisbrecht, S. H. Bossmann, J. Shi, P. Li, *J Biol Chem* **2015**, *290*, 23447-23463; [b]S. Mendes, V. Brissos, A. Gabriel, T. Catarino, D. L. Turner, S. Todorovic, L. O. Martins, *Arch Biochem Biophys* **2015**, *574*, 99-107; [c]S. Mendes, T. Catarino, C. Silveira, S. Todorovic, L. O. Martins, *Catal Sci Technol* **2015**, *5*, 5196-5207.

[16] [a]A. Henriksen, D. J. Schuller, K. Meno, K. G. Welinder, A. T. Smith, M. Gajhede, *Biochemistry* **1998**, *37*, 8054-8060; [b]K. H. Sharp, M. Mewies, P. C. Moody, E. L. Raven, *Nat Struct Biol* **2003**, *10*, 303-307; [c]K. H. Sharp, P. C. Moody, K. A. Brown, E. L. Raven, *Biochemistry* **2004**, *43*, 8644-8651; [d]A. Gumiero, E. J. Murphy, C. L. Metcalfe, P. C. Moody, E. L. Raven, *Arch Biochem Biophys* **2010**, *500*, 13-20.

[17] T. Yoshida, H. Tsuge, H. Konno, T. Hisabori, Y. Sugano, *FEBS J* **2011**, *278*, 2387-2394.

[18] [a]W. A. Doyle, W. Blodig, N. C. Veitch, K. Piontek, A. T. Smith, *Biochemistry* **1998**, *37*, 15097-15105; [b]M. Perez-Boada, F. J. Ruiz-Duenas, R. Pogni, R. Basosi, T. Choinowski, M. J. Martinez, K. Piontek, A. T. Martinez, *J Mol Biol* **2005**, *354*, 385-402.

[19] [a]R. Pogni, M. C. Baratto, S. Giansanti, C. Teutloff, J. Verdin, B. Valderrama, F. Lendzian, W. Lubitz, R. Vazquez-Duhalt, R. Basosi, *Biochemistry* **2005**, *44*, 4267-4274; [b]R. Pogni, M. C. Baratto, C. Teutloff, S. Giansanti, F. J. Ruiz-Duenas, T. Choinowski, K. Piontek, A. T. Martinez, F. Lendzian, R. Basosi, *J Biol Chem* **2006**, *281*, 9517-9526; [c]F. J. Ruiz-Duenas, R. Pogni, M. Morales, S. Giansanti, M. J. Mate, A. Romero, M. J. Martinez, R. Basosi, A. T. Martinez, *J Biol Chem* **2009**, *284*, 7986-7994; [d]A. T. Smith, W. A. Doyle, P. Dorlet, A. Ivancich, *Proc Nat Acad Sci USA* **2009**, *106*, 16084-16089.

[20] Y. Miki, F. R. Calvino, R. Pogni, S. Giansanti, F. J. Ruiz-Duenas, M. J. Martinez, R. Basosi, A. Romero, A. T. Martinez, *J Biol Chem* **2011**, *286*, 15525-15534.

[21] [a]E. Strittmatter, C. Liers, R. Ullrich, S. Wachter, M. Hofrichter, D. A. Plattner, K. Piontek, *J Biol Chem* **2013**, *288*, 4095-4102; [b]E. Strittmatter, S. Wachter, C. Liers, R. Ullrich, M. Hofrichter, D. A. Plattner, K. Piontek, *Arch Biochem Biophys* **2013**, *537*, 161-167.

[22] [a]B. J. Reeder, F. Cutruzzola, M. G. Bigotti, R. C. Hider, M. T. Wilson, *Free Radic Biol Med* **2008**, *44*, 274-283; [b]B. J. Reeder, M. Grey, R. L. Silaghi-Dumitrescu, D. A. Svistunenko, L. Bulow, C. E. Cooper, M. T. Wilson, *J Biol Chem* **2008**, *283*, 30780-30787.

[23] [a]D. Linde, R. Pogni, M. Canellas, F. Lucas, V. Guallar, M. C. Baratto, A. Sinicropi, V. Saez-Jimenez, C. Coscolin, A. Romero, F. J. Medrano, F. J. Ruiz-Duenas, A. T. Martinez, *Biochem J* **2015**, *466*, 253-262; [b]R. Shrestha, X. Chen, K. X. Ramyar, Z. Hayati, E. A. Carlson, S. H. Bossmann, L. Song, B. V. Geisbrecht, P. Li, *ACS Catal* **2016**, *6*, 8036-8047.

[24] M. L. Petrus, E. Vijgenboom, A. K. Chaplin, J. A. Worrall, G. P. van Wezel, D. Claessen, *Open Biol* **2016**, *6*.

[25] A. K. Chaplin, M. T. Wilson, J. A. R. Worrall, *Dalton Trans* **2017**, *46*, 9420-9429.

[26] D. A. Svistunenko, C. E. Cooper, *Biophys J* **2004**, *87*, 582-595.

[27] A. K. Chaplin, C. Bernini, A. Sinicropi, R. Basosi, J. A. R. Worrall, D. A. Svistunenko, *Angew Chem Int Ed Engl* **2017**, *56*, 6502-6506.

[28] D. Kekilli, T. Moreno-Chicano, A. K. Chaplin, S. Horrell, F. S. N. Dworkowski, J. A. R. Worrall, R. W. Strange, M. A. Hough, *IUCrJ* **2017**, *4*, 263-270.

[29] T. Yoshida, H. Tsuge, T. Hisabori, Y. Sugano, *FEBS Letts* **2012**, *586*, 4351-4356.

[30] [a]C. E. Schulz, P. W. Devaney, H. Winkler, P. G. Debrunner, N. Doan, R. Chiang, R. Rutter, L. P. Hager, *FEBS Letts* **1979**, *103*, 102-105; [b]R. Rutter, L. P. Hager, H. Dhonau, M. Hendrich, M. Valentine, P. Debrunner, *Biochemistry* **1984**, *23*, 6809-6816.

[31] B. S. Rajagopal, A. N. Edzuma, M. A. Hough, K. L. Blundell, V. E. Kagan, A. A. Kapralov, L. A. Fraser, J. N. Butt, G. G. Silkstone, M. T. Wilson, D. A. Svistunenko, J. A. Worrall, *Biochem J* **2013**, *456*, 441-452.

[32] D. A. Svistunenko, M. T. Wilson, C. E. Cooper, *Biochim Biophys Acta* **2004**, *1655*, 372-380.
[33] D. Svistunenko, **2004**, https://svistunenko.essex.ac.uk/lev1/tyrdb/home.shtml
[34] C. A. Bonagura, B. Bhaskar, H. Shimizu, H. Li, M. Sundaramoorthy, D. E. McRee, D. B. Goodin, T. L. Poulos, *Biochemistry* **2003**, *42*, 5600-5608.
[35] [a]M. J. Benecky, J. E. Frew, N. Scowen, P. Jones, B. M. Hoffman, *Biochemistry* **1993**, *32*, 11929-11933; [b]W. R. Patterson, T. L. Poulos, D. B. Goodin, *Biochemistry* **1995**, *34*, 4342-4345; [c]A. Khindaria, S. D. Aust, *Biochemistry* **1996**, *35*, 13107-13111; [d]A. Ivancich, H. M. Jouve, B. Sartor, J. Gaillard, *Biochemistry* **1997**, *36*, 9356-9364; [e]T. Matsui, S. Ozaki, Y. Watanabe, *J Am Chem Soc* **1999**, *121*, 9952-9957; [f]A. Hillar, B. Peters, R. Pauls, A. Loboda, H. Zhang, A. G. Mauk, P. C. Loewen, *Biochemistry* **2000**, *39*, 5868-5875; [g]A. Ivancich, G. Mazza, A. Desbois, *Biochemistry* **2001**, *40*, 6860-6866; [h]A. Ivancich, C. Jakopitsch, M. Auer, S. Un, C. Obinger, *J Am Chem Soc* **2003**, *125*, 14093-14102.
[36] D. L. Williams-Smith, R. C. Bray, M. J. Barber, A. D. Tsopanakis, S. P. Vincent, *Biochem J* **1977**, *167*, 593-600.
[37] D. A. Svistunenko, R. P. Patel, S. V. Voloshchenko, M. T. Wilson, *J Biol Chem* **1997**, *272*, 7114-7121.
[38] [a]D. A. Svistunenko, A. Rob, A. Ball, J. Torres, M. C. Symons, M. T. Wilson, C. E. Cooper, *Biochim Biophys Acta* **1999**, *1434*, 74-85; [b]B. J. Reeder, D. A. Svistunenko, C. E. Cooper, M. T. Wilson, *J Am Chem Soc* **2012**, *134*, 7741-7749.
[39] N. Kelso King, F. Looney, M. Winfield, *Biochim Biophys Acta* **1967**, *133*, 65-82.
[40] M. R. Gunther, B. E. Sturgeon, R. P. Mason, *Free Radic Biol Med* **2000**, *28*, 709-719.
[41] H. Miki, K. Harada, I. Yamazaki, M. Tamura, H. Watanabe, *Arch Biochem Biophys* **1989**, *275*, 354-362.
[42] P. K. Witting, A. G. Mauk, *J Biol Chem* **2001**, *276*, 16540-16547.
[43] D. A. Svistunenko, *Biochim Biophys Acta* **2005**, *1707*, 127-155.
[44] M. K. Thompson, S. Franzen, R. A. Ghiladi, B. J. Reeder, D. A. Svistunenko, *J Am Chem Soc* **2010**, *132*, 17501-17510.
[45] C. Bernini, E. Arezzini, R. Basosi, A. Sinicropi, *J Phys Chem B* **2014**, *118*, 9525-9537.
[46] D. von Stetten, T. Giraud, P. Carpentier, F. Sever, M. Terrien, F. Dobias, D. H. Juers, D. Flot, C. Mueller-Dieckmann, G. A. Leonard, D. de Sanctis, A. Royant, *Acta Crystallogr D* **2015**, *71*, 15-26.
[47] S. Monaco, E. Gordon, M. W. Bowler, S. Delageniere, M. Guijarro, D. Spruce, O. Svensson, S. M. McSweeney, A. A. McCarthy, G. Leonard, M. H. Nanao, *J Appl Crystallogr* **2013**, *46*, 804-810.
[48] P. R. Evans, G. N. Murshudov, *Acta Crystallogr D* **2013**, *69*, 1204-1214.
[49] G. N. Murshudov, A. A. Vagin, E. J. Dodson, *Acta Crystallogr D* **1997**, *53*, 240-255.
[50] P. Emsley, B. Lohkamp, W. G. Scott, K. Cowtan, *Acta Crystallogr D* **2010**, *66*, 486-501.
[51] I. W. Davis, A. Leaver-Fay, V. B. Chen, J. N. Block, G. J. Kapral, X. Wang, L. W. Murray, W. B. Arendall, 3rd, J. Snoeyink, J. S. Richardson, D. C. Richardson, *Nucleic Acids Res* **2007**, *35*, W375-383.
[52] O. B. Zeldin, M. Gerstel, E. F. Garman, *J Appl Crystallogr* **2013**, *46*, 1225-1230.
[53] K. S. D. Kumar, M. Gurusaran, S. N. Satheesh, P. Radha, S. Pavithra, K. P. S. T. Tharshan, J. R. Helliwell, K. Sekar, *J Appl Crystallogr* **2015**, *48*, 939-942.
[54] D. A. Svistunenko, N. Davies, D. Brealey, M. Singer, C. E. Cooper, *Biochim Biophys Acta* **2006**, *1757*, 262-272.

[55] M. J. Nilges, K. Matteson, R. L. Bedford, in *ESR Spectroscopy in Membrane Biophysics. Biological Magnetic Resonance, Vol. 27* (Eds.: M. A. Hemminga, L. Berliner), Springer, New York, **2007**, pp. 261-281.
[56] N. A. Baker, D. Sept, S. Joseph, M. J. Holst, J. A. McCammon, *Proc Nat Acad Sci USA* **2001**, *98*, 10037-10041.
[57] D. A. Svistunenko, G. A. Jones, *Phys Chem Chem Phys* **2009**, *11*, 6600-6613.

Table 1: Crystallographic data processing and refinement statistics for ferric DtpA. Helical dataset measured at the ESRF beamline ID30A-3, using a wavelength of 0.9677 Å and an Eiger-4M detector (Dectris).

Space group	$P2_1$
Unit cell (Å, °)	a=60.1, b=71.0, c=78.1; β=92.83
Resolution (Å)	40.20 – 1.41 (1.46 – 1.41)
R_{meas}	0.140 (1.358)
Unique reflections	118339 (9905)
I/σ(I)	7.8 (1.0)
$CC_{1/2}$	0.997 (0.529)
Completeness (%)	93.9 (80.4)
Multiplicity	5.2 (5.1)
R_{factor} (%)	18.9
R_{free} (%)	21.6
RMSD bond lengths (Å)	0.011
RMSD bond angles (°)	1.5
Ramachandran favoured (%)	97.0
Absorbed dose (kGy)	12
PDB accession code	6gzw

Table 2: Phenol ring rotation angle (θ) for the three Tyr residues of ferric DtpA.

	Angle θ^* for $H_{\beta 1}$	Difference with θ = 56°	Difference with θ = 62°
Tyr288	55.0 ± 0.6	1.0	7.0
Tyr374	59.6 ± 0.5	3.6	2.4
Tyr437	59.3 ± 1.9	3.3	2.7

* The average θ value over chains A and B in the crystallographic asymmetric unit

Table 3: Second-order rate constants and steady-state kinetic parameters determined for DtpA and Tyr variants at pH 5 and 25 ºC.

Compound I formation		ABTS			
DtpA	k_1 ($M^{-1}s^{-1}$)	k_{cat} (s^{-1})	K_m (mM)	k_2 ($M^{-1}s^{-1}$)	k_3 ($M^{-1}s^{-1}$)
[a]WT	[a]8.9 (± 0.3) x 10^6	[a]1.1 (± 0.02)	[a]0.7 (± 0.04)	[a]8.8 (± 0.4) x 10^5	[a]1.0 (± 0.1) x 10^3
Y288F	8.7 (± 0.4) x 10^{-6}	1.3 (± 0.03)	1.3 (± 0.08)	11.3 (± 0.3) x 10^5	1.1 (± 0.01) x 10^3
Y374F	9.4 (± 0.3) x 10^6	1.8 (± 0.06)	6.3 (± 0.6)	5.3 (± 0.3) x 10^5	0.4 (± 0.03) x 10^3
Y437F	8.8 (± 0.5) x 10^6	1.5 (± 0.1)	1.8 (± 0.3)	6.0 (± 0.7) x 10^5	1.1 (± 0.02) x 10^3

[a]Data taken from reference 25.

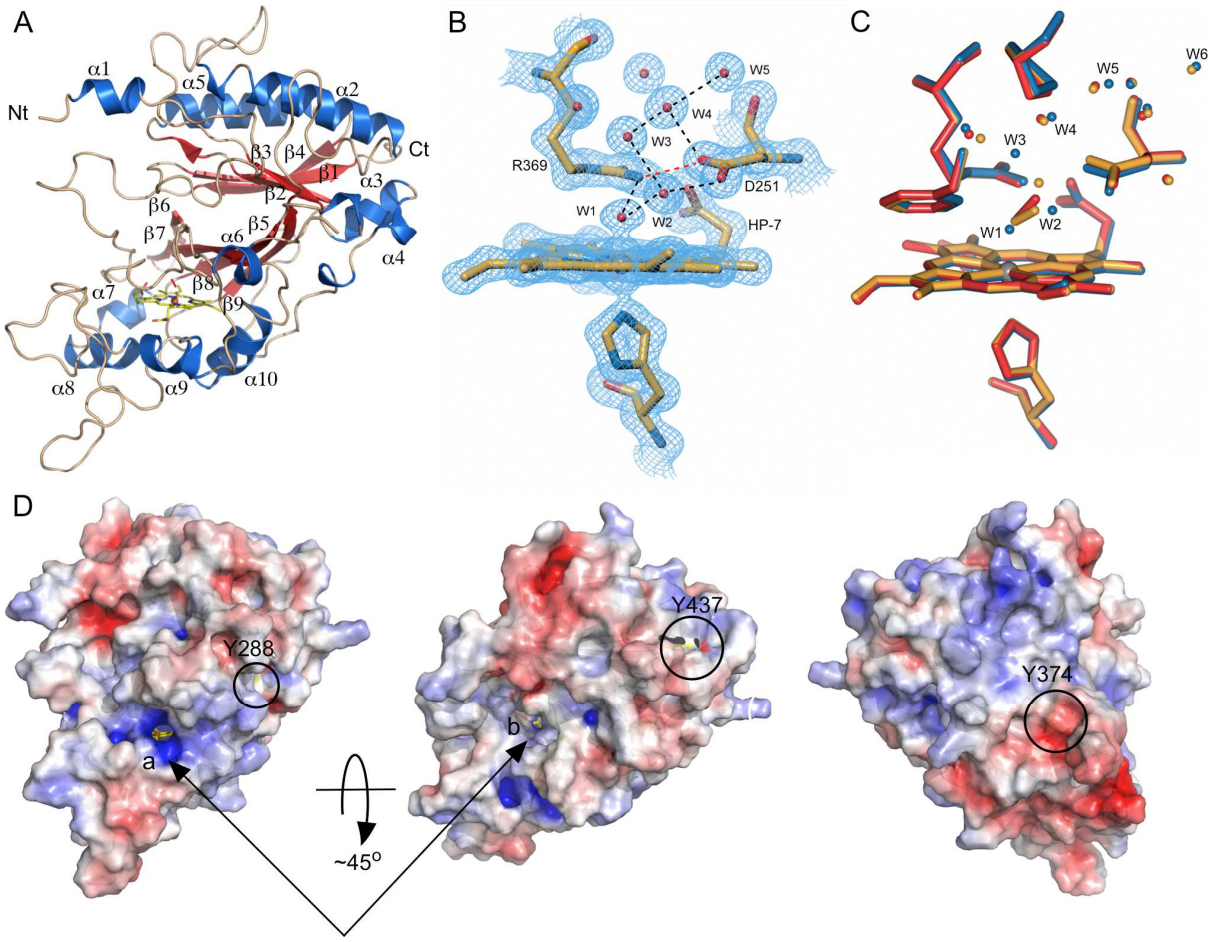

Figure 1: X-ray structure of ferric DtpA. A) Cartoon representation of the tertiary structure of DtpA. Helices and β-strands comprising the two ferredoxin-like domains and the N and C termini are labelled. The heme is drawn in sticks. B) A $2F_o$-F_c electron density map contoured at 1 σ (0.4639 e/Å^3) of the heme region of ferric DtpA, illustrating the bound water molecule to the heme iron and the well-ordered network of distal waters lead to bulk solvent. H-bond (black dash) and salt-bridge (red dash) interactions found in the distal pocket involving the conserved Asp251 and Arg369 residues are indicated. Interactions between Arg 369 and a heme propionate are omitted from the figure for clarity. The distance between the propionate O2A atom and the Nη1 and Nη2 atoms of Arg 369 are 2.84 and 2.83 Å, respectively in monomer A, and 3.04 and 2.71 Å, respectively in monomer B. C) Comparison between the DtpA ferric species (blue), the photoreduced oxy-ferrous species (red; 5MAP), and a partially photo-reduced mixed species (orange; 5MJH). The O-O bound to the heme iron is represented as a stick. D) Electrostatic surface calculated at pH 7 using APBS.[56] The orientation of DtpA depicted on the left-hand side is the same as in (A). Access sites to the heme from the surface are labelled *a* and *b*. The location of the three Tyr residues are indicated.

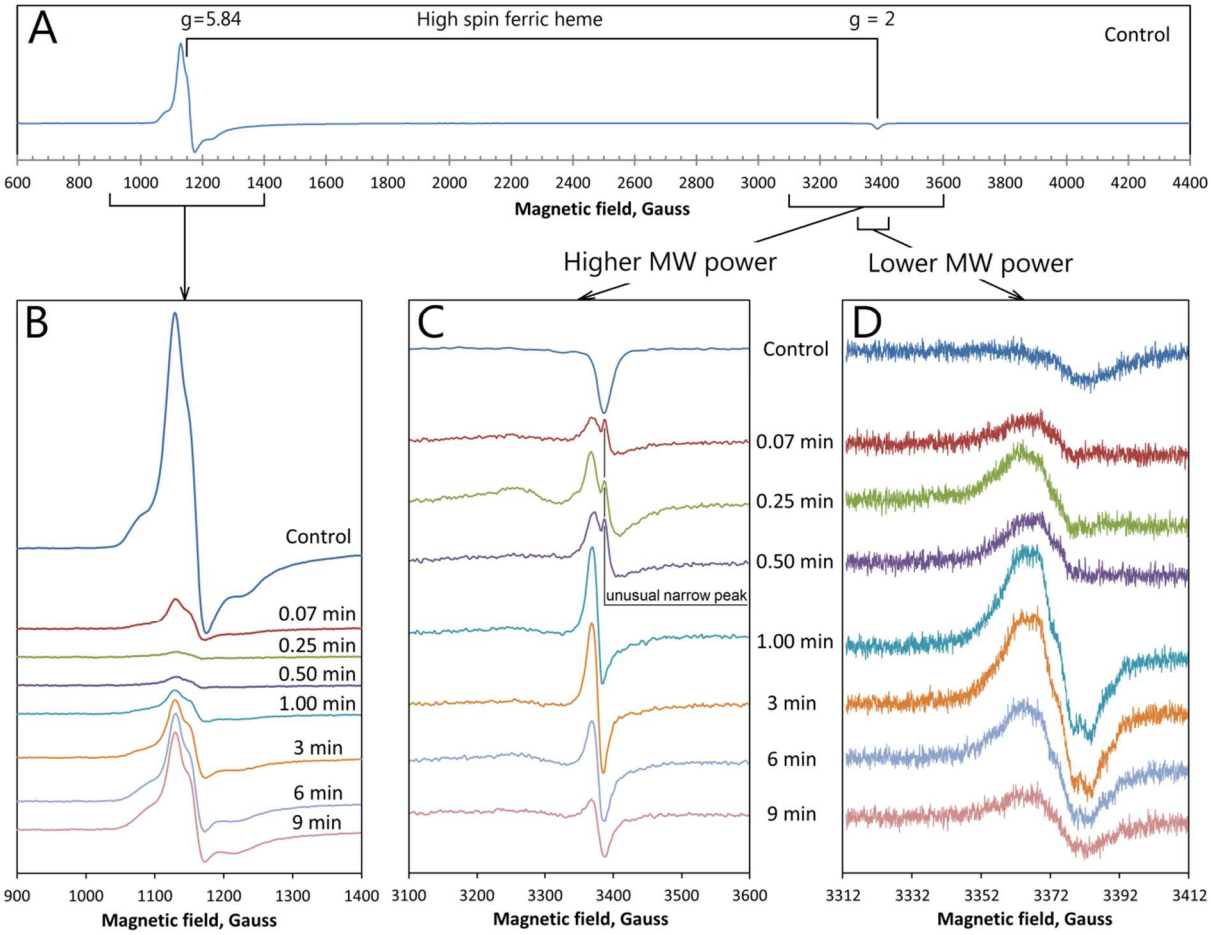

Figure 2: Low temperature (T = 10 K) EPR spectra of WT DtpA before and after addition of H_2O_2 at pH 5. A) 40 µM DtpA (the *Control*) measured at the following instrumental conditions: microwave power P_{MW} = 3.18 mW; microwave frequency ν = 9.466 GHz; modulation amplitude A_m = 5 G; modulation frequency ν_m = 100 kHz; time constant τ = 82 ms; sweep rate v = 22.65 G/s; number of scans NS = 1. Addition of H_2O_2 to produce the final concentrations of 40 µM DtpA and 400 µM H_2O_2 ([DtpA]/[H_2O_2] = 1:10), results in the spectral changes over the times reported in (B), (C) and (D) for different magnetic field ranges (indicated). (B) Instrumental conditions were as in (A) but a smaller field range is reported to highlight the perpendicular components of the g-tensor of the high spin ferric heme (at g~6). (C) The free radical region of the spectrum measured at the same instrumental conditions as (A) but for a smaller field width and ν = 9.467 GHz; A_m = 3 G; v = 0.60 G/s. (D) Narrower magnetic field focusing on the free radical EPR signal as detected at a lower microwave power (P_{MW} = 0.05 mW). The background signal recorded for a blank (water) sample has been subtracted from every spectrum.

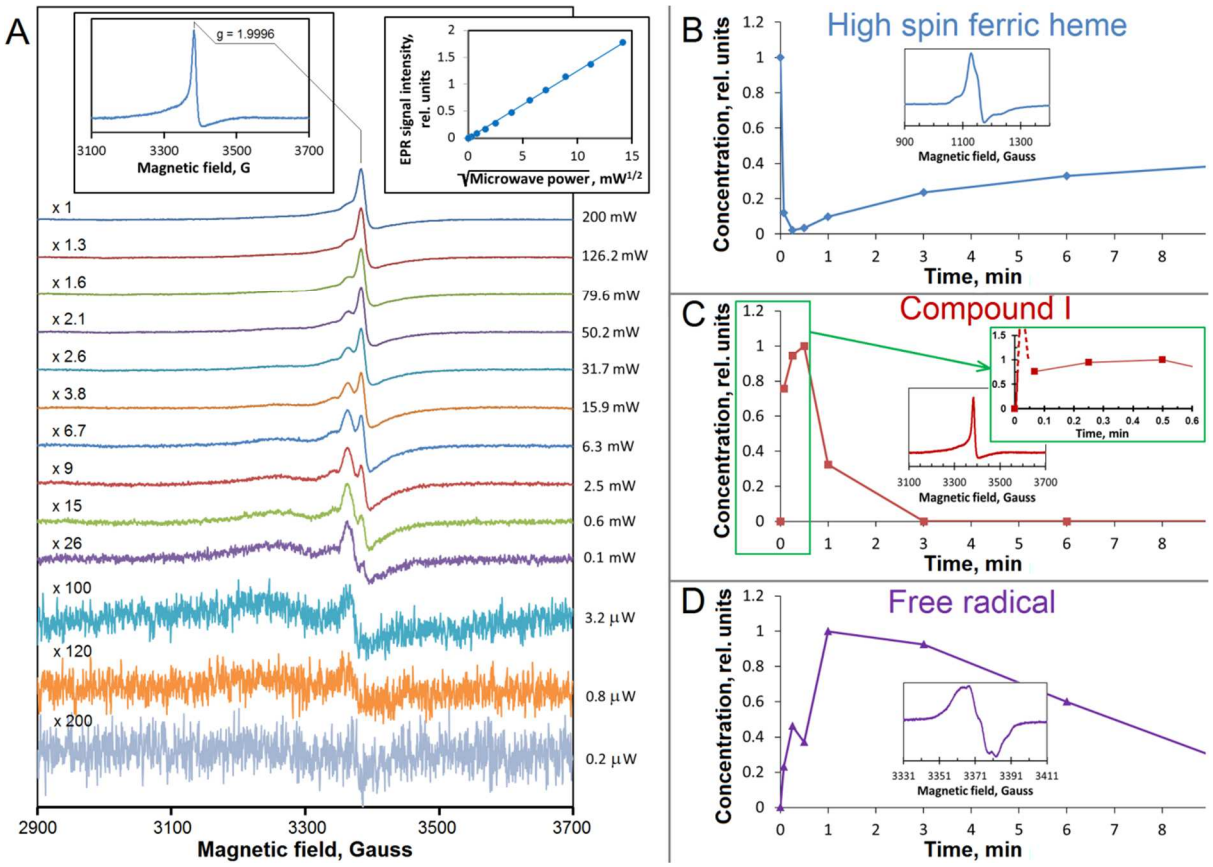

Figure 3: Extraction of Compound I EPR line shape and kinetic dependences of the three species. A) The pure line shape (*top left inset*) of the EPR signal assigned to Compound I in DtpA, frozen 4 s after addition of H_2O_2, and its microwave power saturation behavior. Both protein and H_2O_2 final concentrations were 80 µM, pH 5. The instrumental parameters different from those in Fig. 2 were ν = 9.468 GHz, A_m = 3 G, v = 4.77 G/s. The pure line shape of the Compound I spectrum was obtained as a difference spectrum ((126.2 mW) - 0.885 x (50.2 mW)). This pure line shape has been used to determine the intensity of the signal in every spectrum by subtraction with variable coefficient [54]; the coefficient values were then used to plot the dependence of the Compound I EPR signal on (microwave power)$^{1/2}$ (*top right inset).* B-D) Kinetic dependences of the 3 paramagnetic species identified in the DtpA EPR spectra shown in Fig. 2. The relative unit 1.00 for the ferric heme concentration in (B) and the free radical concentration in (D) correspond to 40 µM and 0.5 µM, respectively. For Compound I in (C), only an approximate concentration of ~ 0.44 µM can be estimated for its relative unit 1.00 due to the wide wings of the EPR signal and the 3 principal g-values not accurately determined. The *inset EPR spectra* show the pure line shape EPR signals of the 3 species: (B) the control spectrum in Fig. 2B, (C) Compound I spectrum as in *top left inset* in (A), and (D) the free radical EPR spectrum recorded at T =15 K and the instrumental parameters specified

in Fig. 2D for 80 μM DtpA mixed with 800 μM H_2O_2 and frozen 2.25 min thereafter. The *inset outlined green* in (C) shows the expanded interval of the Compound I kinetic dependence of 0 to 0.6 min with a speculated course of the curve (dashed line) earlier than the first experimental point of 4 s (see main text).

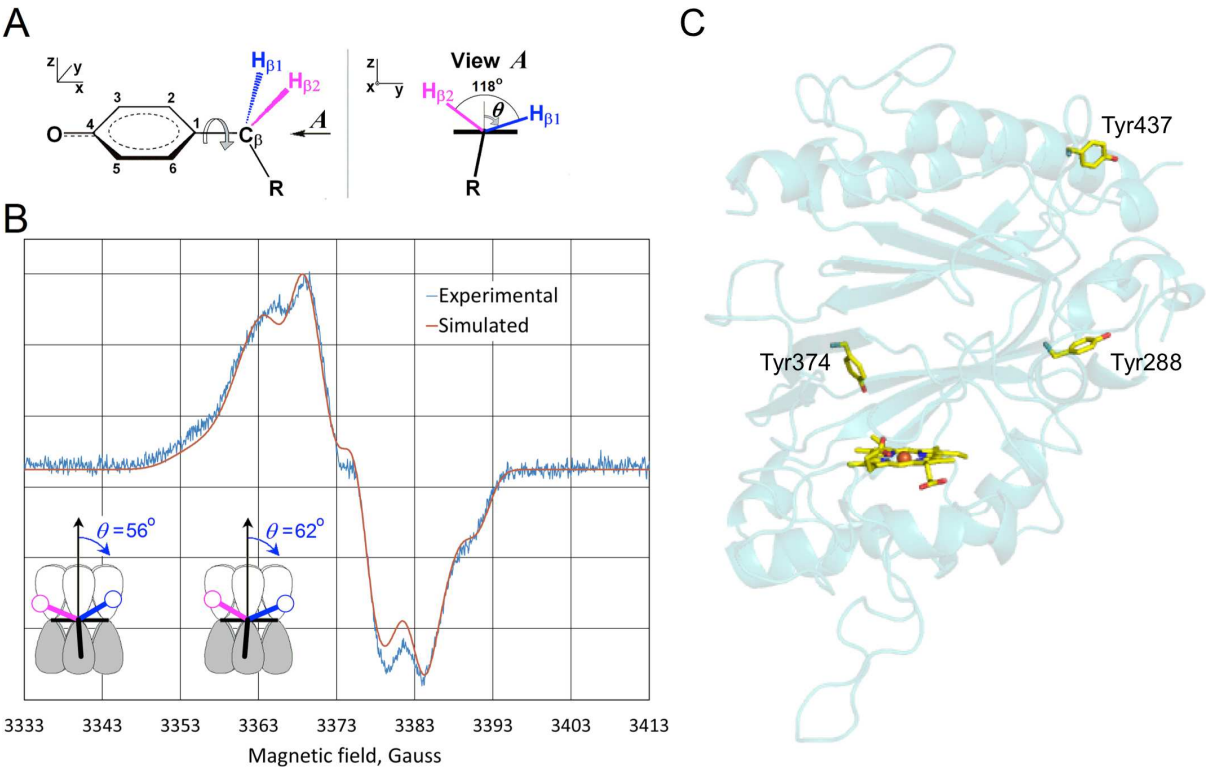

Figure 4: Simulation of the DtpA radical EPR spectrum. A) Schematic of a Tyr radical structure, with atoms nomenclature, and the definition of the ring rotation angle, θ. Note that the angle between the two methylene protons is 118°, not 120° expected from symmetry considerations, as follows from the DFT calculations.[57] B) TRSSA-Y.v2 assisted simulation of the DtpA protein-bound radical. The experimental spectrum (pH 5) was obtained as a difference of two spectra, measured at two different microwave power values, of the same sample, 80 µM DtpA mixed with 800 µM H_2O_2 and frozen 3 min thereafter: [0.05 mW] – 0.17 x [3.18 mW] (the 0.17 factor was chosen empirically to minimise the least readily saturating spectral components). The parameters used to simulate the spectrum were generated by TRSSA-Y.v2 for an optimal input of ρ_{C1} = 0.38 and θ = 56° (or θ = 62°, the complimentary to 56° angle that gives identical simulation parameters) and are specified in Table S1. C) Location of the three Tyr residues in DtpA relative to the heme.

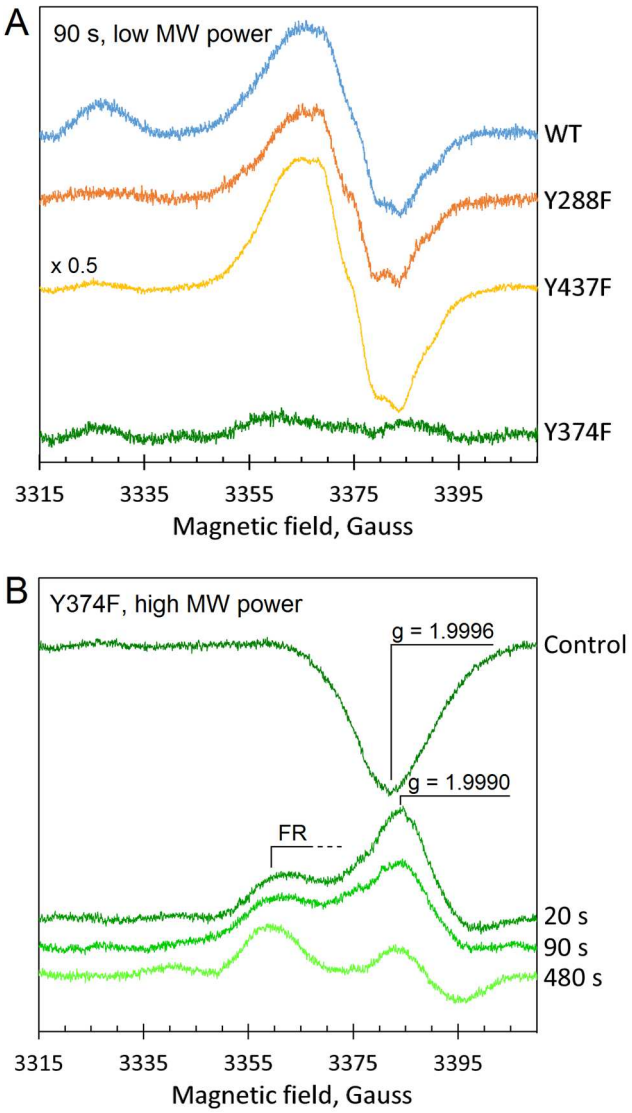

Figure 5: The free radical region of the EPR spectra of DtpA Tyr variants. A) Low microwave power (P_{MW} = 0.05 mW) EPR spectra of the four DtpA proteins at pH 5.0 frozen 90 s after addition of H_2O_2 and corresponding to the maximal concentration of free radical in the WT, Y288F and Y437F. For the Y374F variant no protein-bound radical species at a concentration above the noise is observed. The Y437F spectrum was multiplied by a factor of 0.5. B) The Y374F free radical region with samples frozen at times indicated following activation with H_2O_2. The unusual line shape of this free radical region spectrum is caused by the presence of the Compound I signal (maximum at g=1.9990). The g=1.9996 line in the control (no H_2O_2 added) is the parallel component on the HS ferric heme EPR signal. The signal labelled FR coincides with the position of where the free radical EPR signal should be observed. Spectra were recorded with a microwave power of P_{MW} = 3.16 mW. In A and B the instrumental parameters are as follows; ν = 9.4656 GHz; A_m = 3 G; ν_m = 100 kHz; τ = 82 ms; v = 0.60 G/s; NS = 1; T= 10 K.

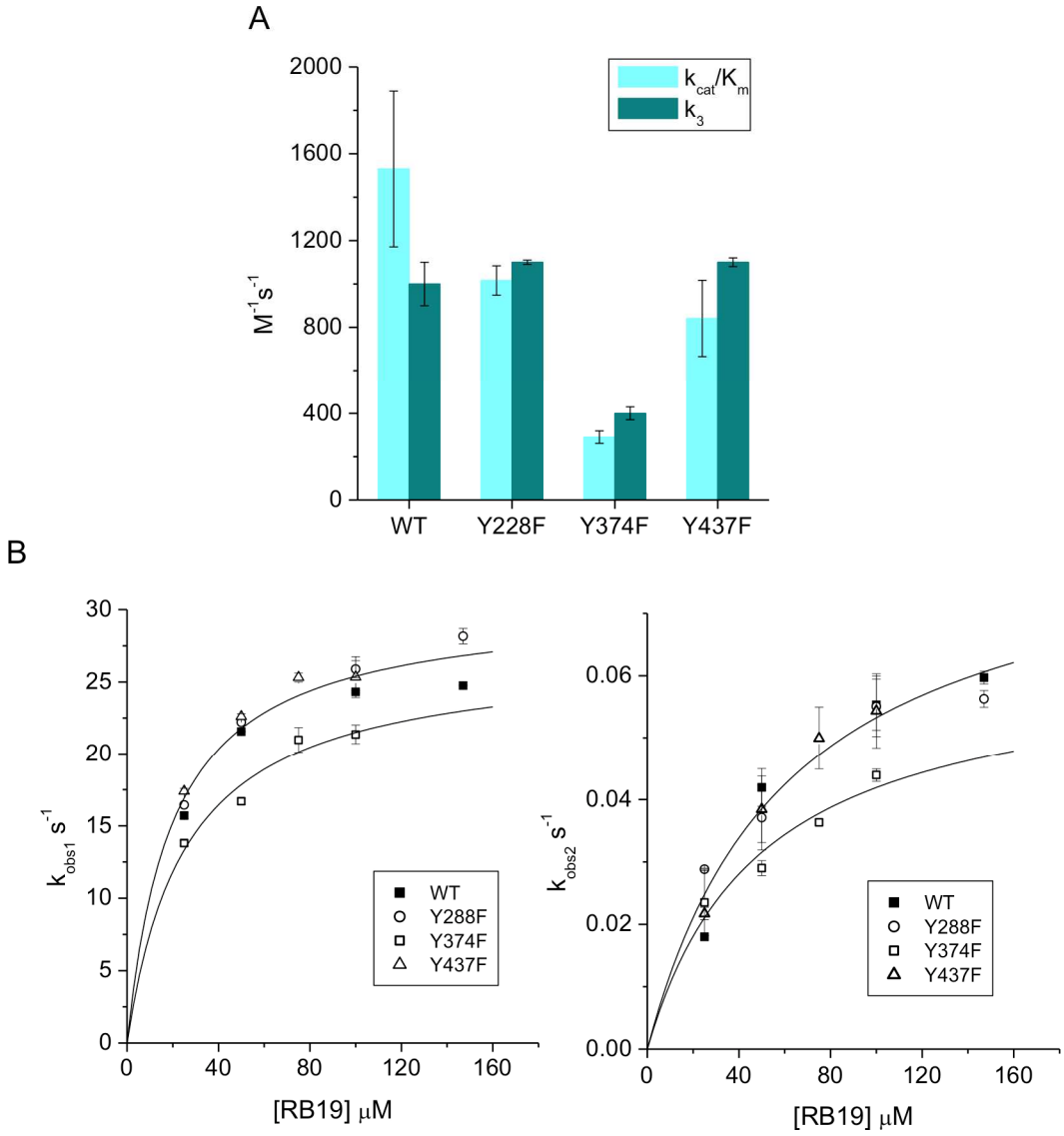

Figure 6: Oxidative kinetics of DtpA and Tyr variants with ABTS and RB19. A) Comparison of the catalytic efficiency (k_{cat}/K_m) determined from steady-state kinetics and the second-order rate constant, k_3, determined from stopped-flow kinetics for the oxidation of ABTS. B) Observed pseudo first-order rate constants plotted against RB19 concentrations for the fast phase (k_{obs1}) and slow phase (k_{obs2}) measured at 420 nm. Data points are fitted to a hyperbola.

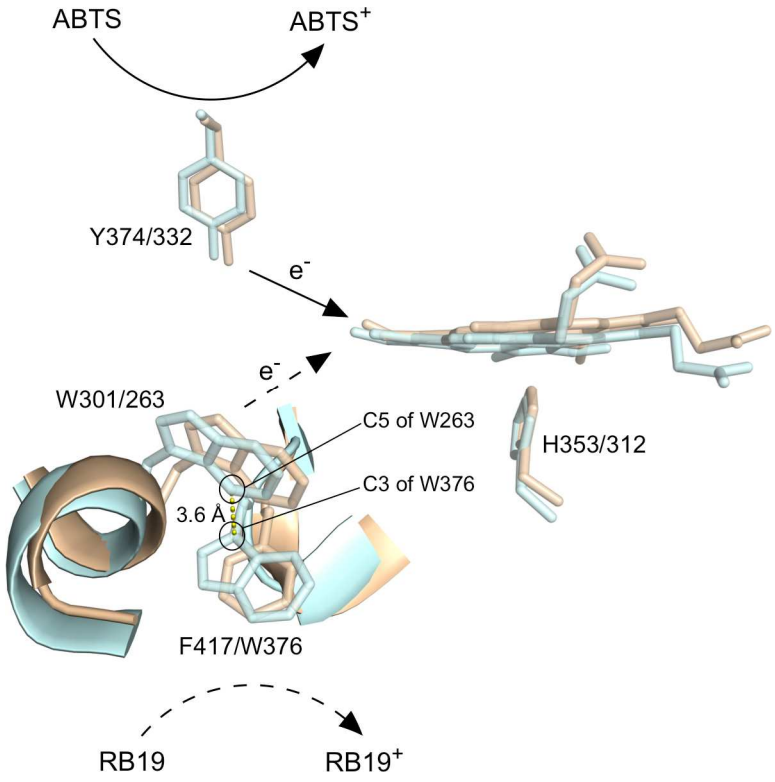

Figure 7: The Trp dyad. Structural superpositions of ferric DtpA (wheat) and *Tc*DyP (pale cyan, pdb ID 5JXU) with the Trp and Tyr residues determined to be radical sites in both proteins indicated (DtpA/*Tc*DyP numbering). The shortest distance between the Trp dyad in *Tc*DyP is indicated by the dashed yellow line and the C5 and C3 indole ring atoms are indicated. ET pathways for ABTS and RB19 are illustrated with solid and dashed lines, respectively.

Graphical abstract

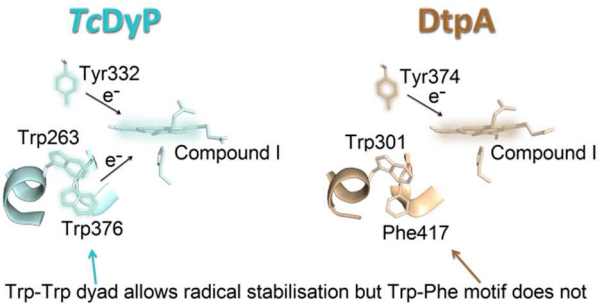

Aromatic redox motifs: In the dye decolourising heme peroxidase family an aromatic redox motif is proposed to facilitate an electron transfer pathway from anthraquinone-based dye substrates to the high-valent iron(IV)-oxo species. In its absence reactivity with synthetic dyes is impaired.